Diffusion Directions Imaging (DDI)

Aymeric Stamm, Patrick Pérez, Christian Barillot

INSTITUT NATIONAL DE RECHERCHE EN INFORMATIQUE ET EN AUTOMATIQUE

Diffusion Directions Imaging (DDI)

Aymeric Stamm* — Patrick Pérez† — Christian Barillot*

N° 7683 — version 2

initial version July 2011 — revised version September 2011

Computational Medicine and Neurosciences

ISSN 0249-6399 ISRN INRIA/RR--7683--FR+ENG

INSTITUT NATIONAL
DE RECHERCHE
EN INFORMATIQUE
ET EN AUTOMATIQUE

INRIA

centre de recherche
RENNES - BRETAGNE ATLANTIQUE

Diffusion Directions Imaging (DDI)

Aymeric Stamm* , Patrick Pérez† , Christian Barillot*

Theme : Computational Medicine and Neurosciences
Computational Sciences for Biology, Medicine and the Environment
Équipe-Projet *VisAGeS
†Technicolor Research & Innovation

Rapport de recherche n° 7683 — version 2 — initial version July 2011 —
revised version September 2011 — 28 pages

Abstract: Diffusion magnetic resonance imaging (dMRI) is the reference *in vivo* modality to study the connectivity of the brain white matter. Images obtained through dMRI are indeed related to the probability density function (pdf) of displacement of water molecules subject to restricted diffusion in the brain white matter. The knowledge of this diffusion pdf is therefore of primary importance. Several methods have been devised to provide an estimate of it from noisy dMRI signal intensities. They include popular diffusion tensor imaging (DTI) as well as higher-order methods. These approaches suffer from important drawbacks. Standard DTI cannot directly cope with multiple fiber orientations. Higher-order approaches can alleviate these limitations but at the cost of increased acquisition time. In this research report, we propose, in the same vein as DTI, a new parametric model of the diffusion pdf with a reasonably low number of parameters, the estimation of which does not require acquisitions longer than those used in clinics for DTI. This model also accounts for multiple fiber orientations. It is based on the assumption that, in a voxel, diffusing water molecules are divided into compartments. Each compartment is representative of a specific fiber orientation (which defines two opposite directions). In a given compartment, we further assume that water molecules that diffuse along each direction are in equal proportions. We then focus on modeling the pdf of the displacements of water molecules that diffuse only along one of the two directions. Under this model, we derive an analytical relation between the dMRI signal intensities and the parameters of the diffusion pdf. We exploit it to estimate these parameters from noisy signal intensities. We carry out a cone-of-uncertainty analysis to evaluate the accuracy of the estimation of the fiber orientations and we evaluate the angular resolution of our method. Finally, we show promising results on real data and propose a visualization of the diffusion parameters which is very informative to the neurologist.

Key-words: diffusion magnetic resonance imaging, imaging biomarkers, von Mises & Fisher distribution, brain white matter modeling

Centre de recherche INRIA Rennes – Bretagne Atlantique
IRISA, Campus universitaire de Beaulieu, 35042 Rennes Cedex
Téléphone : +33 2 99 84 71 00 — Télécopie : +33 2 99 84 71 71

Diffusion Directions Imaging (DDI)

Résumé : Diffusion magnetic resonance imaging (dMRI) est la modalite de reference pour etudier les connectivites dans la matiere blanche du cerveau. Les images obtenues par dMRI sont en effet liees a la densite de probabilite du deplacement des molecules d eau sujettes a une diffusion contrainte dans la matiere blanche. La connaissance de cette densite, appelee densite de diffusion, est par consequent d une importance capitale. N etant pas mesurable, de nombreuses methodes ont ete imaginees pour l estimer a partir d images bruitees produites par dMRI. Parmi elles, on compte le populaire modele DTI ainsi que des methodes d ordres superieurs. Ces approches souffrent d importants inconvenients. Le modele DTI standard ne peut pas directement gerer plusieurs orientations de fibres. Les methodes d ordres superieurs soulagent cette limitation mais au prix d une augmentation non negligeable du temps d acquisition. Dans ce rapport de recherche, nous proposons, dans la meme veine que DTI, un nouveau modele parametrique pour la densite de diffusion avec un nombre raisonnablement faible de parametres dont l estimation ne requiert pas d acquisitions plus longue que celles faites pour DTI. Ce nouveau modele prend aussi en compte differentes orientations de fibres possibles. Il est base sur l hypothese que, dans un voxel, les molecules d eau sujettes a la diffusion sont divisees en plusieurs compartiments. Chaque compartiment represente une orientation de fibres donnee (ce qui definit deux directions opposees). Dans un compartiment donne, nous faisons l hypothese supplementaire que les molecules d eau diffusent dans chacune de ces deux directions en proportions egales. Ceci nous permet de nous concentrer sur la modelisation de la densite de deplacement des molecules d eau uniquement le long d une direction. En substance, nous la modelisons par la convolution d une Gaussienne 3D et d une densite de von Mises & Fisher 2D. La premiere est parametree de telle sorte a capturer principalement la composante radiale de la diffusion pendant que la seconde capture la composante angulaire. Un melange equi-pese de deux densites de ce genre avec des directions opposees fournit notre modele mono-compartimental. Un melange de ces densites fournit le modele multi-compartimental qui permet la prise en compte de multiples orientations de fibres. Sous ces hypotheses sur la forme de la densite de diffusion, nous derivons ensuite une relation analytique entre l intensite du signal de diffusion et les parametres de la densite de diffusion. Nous l exploitons pour estimer ces parametres a partir des intensites des signaux de diffusion bruites. Nous menons une analyse par *cone d incertitude* pour evaluer la precision de l estimation des orientations des fibres et nous evaluons la resolution angulaire de notre methode pour un nombre d acquisitions et un niveau de bruit donnes. Enfin, nous montrons des resultats prometteurs sur donnees reelles et proposons une visualisation simple des parametres de diffusion tres informative pour le neurologue.

Mots-clés : diffusion magnetic resonance imaging, biomarqueurs d'imagerie, distribution de von Mises & Fisher, modélisation de la matière blanche cérébrale

Contents

1 Introduction and Motivations **3**

2 Methods **6**
2.1 The new proposed diffusion model 7
2.1.1 Single-compartment model 7
2.1.2 Multi-compartment Model 9
2.2 Estimation of the DDI Parameters 11
2.2.1 Analytical expression of the theoretical diffusion signal . . 11
2.2.2 Asymptotic behaviors 12
2.2.3 Estimation from noisy diffusion signals 12
2.2.4 Model Selection 13

3 Results **14**
3.1 Simulation study 14
3.1.1 Goals 14
3.1.2 Generation of the simulated data sets 14
3.1.3 Analysis 15
3.2 Real data experiments 17

4 Discussion and Conclusion **18**
4.1 Theoretical aspects 18
4.2 Practical aspects 19
.1 Definitions from probability theory 19
.2 The von Mises & Fisher probability distribution 20
.3 Independent sum of a von Mises & Fisher variable and a Gaussian variable 21

1 Introduction and Motivations

Diffusion magnetic resonance imaging (dMRI) [1] allows *in-vivo* and non-invasive investigation of biological tissue structure. A widespread application of dMRI is the study and analysis of the brain white matter constituted of intricate fiber bundles (axons) into which the diffusion of water molecules is restricted: analyzing these restrictions allows one to infer bundles geometry (orientations, diameter, etc).

Standard dMRI sequences are obtained by applying a series of magnetic field gradients $\boldsymbol{q}$ to a subject's brain. Under the *q-space imaging* formalism [2], which we adopt here, the duration δ of the pulse during which each gradient is applied is very short and negligible with respect to (wrt) the diffusion time Δ between two successive applied gradients. Under this assumption, each magnetic field gradient $\boldsymbol{q}$ is constant over its application pulse. It is defined by its 3D direction $\boldsymbol{g}$[1] and its intensity classically encoded by the so-called b value according to [2] $b = (\Delta - \delta/3)\,\|\boldsymbol{q}\|^2$. The q-space is then the set of all possible combination of a direction and a b value.

[1] Throughout the manuscript, the term *direction* refers to a unit 3D vector whereas the term *orientation* refers either to a unit 3D vector or to its opposite indifferently.

Under the *q-space imaging* formalism, in each voxel, we have, for any vector $\boldsymbol{q}$ in the q-space [3, 4]:

$$\frac{A^\star(\boldsymbol{q})}{A^\star(\boldsymbol{0})} = \int_{\mathbb{R}^3} f_{\mathbf{x}}(\boldsymbol{x}) \mathrm{e}^{i\boldsymbol{q}'\boldsymbol{x}} \mathrm{d}\boldsymbol{x} \ , \tag{1}$$

where $A^\star(\boldsymbol{q})$ is the theoretical complex magnetization of all contributing spins [5] after the diffusion time Δ induced by the application of the magnetic field gradient $\boldsymbol{q}$, $\mathbf{x}$ is the 3-dimensional random variable that represents the displacement of the water molecules, $\boldsymbol{x}$ is one realization of it[2] and $f_{\mathbf{x}}$ is the **diffusion probability density function** (pdf).

In practice, for each magnetic field gradient $\boldsymbol{q}$, we measure a **raw diffusion signal** $S(\boldsymbol{q})$ which, in absence of measurement noise, amounts to $A(\boldsymbol{q}) := |A^\star(\boldsymbol{q})|$ (**theoretical diffusion signals**). Two issues arise then: (i) the raw diffusion signals are corrupted by measurement noise, usually assumed to be Rician [6], and (ii) we cannot collect the raw diffusion signals for each point in the q-space and we need to sample the latter by combining a finite set of b values $\{b_k\}_{k\in[\![1,n_b]\!]}$ and a finite set of 3D directions $\{\boldsymbol{g}_j\}_{j\in[\![1,n_g]\!]}$.

Inferring the micro-structure of the tissues consists in reconstructing the diffusion pdf to some extent. Different methods have been devised to this end [7]. They usually rely on the assumption that the distribution of the displacements of water molecules is symmetric, in which case the diffusion pdf is termed the ensemble average propagator (EAP) [8]. They hinge on four major q-space sampling schemes:

Full Sampling. If the q-space is entirely sampled on a Cartesian lattice with sufficient density (so that accurate fast Fourier transform (FFT) can be performed), the model-free Diffusion Spectrum Imaging (DSI) method [9] proposes an accurate reconstruction of the EAP. Assuming the diffusion pdf to be symmetric indeed implies that the normalized theoretical complex magnetization (left part of Eq.(1)) is equal to its modulus, the Fourier transform (FT) of which directly yields the EAP. An estimation of the EAP is thus obtained by FFT of the normalized raw diffusion signals. A full sampling of the q-space however requires a huge number of both encoding b values, including high b values (up to 8000s/mm^2), and encoding directions (up to 500) leading to an acquisition time of several hours [10].

Multi-Shell Imaging (MSI) Sampling. MSI consists in sampling the q-space over a large number of encoding directions (up to 60) uniformly spread on **several** spheres (usually 2-4 b values, both low and high). Even if it significantly reduces the acquisition time wrt to a full sampling, it still takes approximately 30 min. This spherical sampling is not suited to DSI. Adjusting the raw diffusion signal to a Cartesian lattice by means of bilinear interpolation yields Hybrid Diffusion Imaging (HYDI) [11]. Other model-free methods based on MSI sampling provide estimates of the EAP by expanding the raw diffusion signals by means of (i) 4-th order tensors [12, 13], (ii) the spherical polar Fourier basis up to a given order [14, 15], (iii) the solid harmonics basis up to a given order giving its name to Diffusion Propagator Imaging (DPI) [16] or (iv) the Gram-Charlier expansion up to a given order [17]. The latter method is the only that provides

[2] To distinguish a random variable from one realization of it, we adopt a sanserif type to designate the former and a curvilinear type to designate the latter.

an estimate of the diffusion pdf and not only of the EAP. Unfortunately, it requires the use of both the intensity and phase of the complex magnetization. Alternatively, model-dependent methods that assume the diffusion pdf to be a mixture of Gaussian densities (e.g., the "multi-Gaussian" model [18], the "multi-Watson" model [19], and the Ball & Stick model [20]) make use of MSI [21] and provide a parametric estimation of the EAP.

High Angular Resolution Diffusion Imaging (HARDI) Sampling. HARDI consists in sampling the q-space over a large number of encoding directions (up to 60) uniformly spread on a high-radius **single** sphere (single high b value, typically greater than 1500s/mm^2) [22] which further reduces the acquisition time wrt MSI (lower bound of about 15 min). Model-free methods that use HARDI sampling revolve around q-ball imaging (QBI) [23] and diffusion orientation transform (DOT) [24]. Both methods focus on the estimation of some specific angular feature of the EAP, namely the diffusion orientation distribution function (dODF) (to be precise, an approximation thereof) defined as the density of the marginal probability distribution of the molecular displacements on the 2-dimensional unit sphere [25] and the isoradius of the EAP, respectively. QBI originally estimates the dODF by expanding the raw diffusion signals by means of a spherical radial basis function with Gaussian kernel [23]. Further works exhibit a faster and more robust QBI by expanding the raw diffusion signals by means of the spherical harmonics (SH) basis [26, 27, 28]. As for DOT, the isoradius of the EAP is estimated by expanding the Fourier-Bessel transform of the raw diffusion signals by means of the SH basis [24]. The model-dependent methods using HARDI sampling are (i) the composite hindered and restricted mixture model, coined CHARMED [29], of which one component is an isotropic Gaussian density and the others are Neuman-type densities for restricted diffusion within a cylinder [30] which yields a parametric estimation of the EAP and (ii) spherical deconvolution models [31, 32] which estimate the fiber orientation distribution function (fODF). The latter methods assume that the theoretical diffusion signals are the result of the convolution between the fODF, assumed symmetric, and a kernel reflecting the diffusion within a given fiber. This kernel is in turn assumed (i) of Gaussian-type [33, 26, 34], (ii) of Rigaut-type [35] or (iii) sinusoidal [36] (which is an alternative formulation of persistent angular structure MRI (PAS-MRI) [37]). Data-dependent kernels are also proposed in [38, 39, 40].

Low Angular Resolution Diffusion Imaging (LARDI) Sampling. LARDI consists in sampling the q-space over a low number of encoding directions (typically less than 30) uniformly spread on a low-radius **single** sphere (single low b value, typically lower than 1500s/mm^2) so that the acquisition time drops below 10 min. To the best of our knowledge, the only method to date compatible with LARDI sampling is diffusion tensor imaging (DTI) [41]. It is a model-dependent method that provides a parametric estimation of the EAP by assuming the latter to be a 3-dimensional centered Gaussian pdf parametrized by a *diffusion tensor*. The derivation of Eq.(1) is then straightforward and thus the theoretical diffusion signal can be analytically expressed as a function of the diffusion tensor. Unlike all the other methods, DTI does not account for the intra-voxel white matter fiber heterogeneity brought to light in [18].

Clinical protocols often include, in addition to the dMRI sequence, other types of sequences (e.g., 3D T1, FLAIR and T2 for vascular pathologies, perfusion, resting-state, magnetization transfer, etc). Neurologists thus agree with

an upper bound of 10 min for the acquisition time (AT) of the dMRI sequence so that the whole protocol does not exceed half an hour. Even if several recent approaches allow significant reduction of the acquisition time for full sampling or MSI sampling notably by means of compressed sensing [42, 43], they are still prohibitively time-consuming (around 20 min). In a clinical setting, only dMRI data sets acquired with LARDI sampling of the q-space can thus be used to infer the diffusion pdf. In addition, because of the intra-voxel white matter fiber heterogeneity, a method for the reconstruction of the diffusion pdf should account for multiple fiber orientations. Table 1 shows that there is no state-of-the-art method that relies on LARDI sampling of the q-space while coping with several fiber orientations.

Table 1: Summary of the different sampling schemes of the q-space, with estimated lower bound of the acquisition time and indication on whether associated state-of-the-art methods account for multiple fiber orientations or not.

Sampling	AT Lower bound	Multi-fiber
Full	30 min	yes
MSI	20 min	yes
HARDI	15 min	yes
LARDI	10 min	no

The contribution of this work is to propose a new method for the reconstruction of the diffusion pdf, coined diffusion directions imaging (DDI), that fulfills the following three objectives:

1. being compatible with dMRI data sets acquired in **maximum 10 min**,
2. estimating **multiple fiber directions**, and,
3. allowing for the **retrospective analysis of DTI repositories** acquired in the past.

We introduce the new proposed method in Section 2. Then, we validate the method on simulated dMRI data sets and we show its applicability and performances on clinical dMRI data sets in Section 3. Finally, we propose a discussion on both theoretical and practical aspects of the method in Section 4.

2 Methods

The simplest and most widespread method for the reconstruction of the diffusion pdf, which is to date the only used by clinicians to analyze dMRI data sets, is the model-dependent DTI [41]. It assumes that $\mathbf{x} = \sqrt{2\,(\Delta - \delta/3)}\mathbf{y}$, where $\mathbf{y}$ follows a 3-dimensional centered Gaussian probability distribution whose covariance matrix D is termed the *diffusion tensor*. Because of the nature of the Gaussian probability distribution, this method (i) assumes a unique direction of diffusion per voxel and (ii) mixes up the angular and radial components of the diffusion.

Nevertheless, model-dependent methods seem to be the key to reconstructing the diffusion pdf from clinically acquired data sets. Therefore, we propose an alternative parametric probability distribution for the random variable $\mathbf{y}$ to remedy the weaknesses in the DTI method. The random motion of water molecules in the white matter depends on the surrounding tissue structure. Because of the intra-voxel white matter fiber heterogeneity, first brought to light in

[18], we assume that, in each voxel, water molecules can be divided into several compartments.

First, we describe how we model the diffusion within a single compartment and how this model gives access to important characteristics of the diffusion in this compartment (e.g., fiber orientation, associated measure of anisotropy and mean radial displacement). Then, we introduce our multi-compartment model of the diffusion pdf, coined Diffusion Directions Imaging (DDI), of which we propose a motivated parametrization. Second, we propose a method to estimate the parameters of the DDI model from the raw diffusion signals. In particular, (i) we establish the analytical relation between the theoretical diffusion signals and the parameters of the DDI model, (ii) we go into details regarding some interesting asymptotic behaviors of this analytical relation and (iii) we explain how we handle both the inherent measurement noise (which the raw diffusion signals are corrupted with) and the underlying model selection problem to improve the robustness of the estimation.

2.1 The new proposed diffusion model

In this subsection, we refer to the diffusion pdf as the pdf of the random variable $\mathbf{y}$ instead of the pdf of the random molecular displacement $\mathbf{x}$. This can be done without loss of generality since $\mathbf{x}$ and $\mathbf{y}$ differ only from a multiplicative scalar factor $\sqrt{2\,(\Delta - \delta/3)}$, which only depends on times that are constant throughout the sequence of acquisition.

2.1.1 Single-compartment model

Local diffusion modeling. We aim at better separating the angular and radial components of the diffusion while coping with multiple fiber orientation so that we alleviate the limitations of the DTI model.
A compartment regroups water molecules diffusing along a specific fiber orientation $\pm\boldsymbol{\mu}$. It can be further divided into two groups: (i) water molecules that diffuse in the direction $+\boldsymbol{\mu}$ and (ii) water molecules that diffuse in the direction $-\boldsymbol{\mu}$.

Diffusion model along a specific direction of diffusion Let us first focus on modeling the diffusion of water molecules along direction $+\boldsymbol{\mu}$. The random 3-dimensional displacement $\mathbf{w}$ of these water molecules results from the combination of a random 2-dimensional direction and a random 1-dimensional displacement along that direction.
Ideally, one could think of expressing the random variable $\mathbf{w}$ in spherical coordinates as $\mathbf{w} = r\mathbf{v}$ so that both the radial component (r) and the angular component ($\mathbf{v}$) are explicitly modeled. However, to the best of our knowledge, there is no pair of known parametric probability distributions (a univariate one on $\mathbb{R}^+$ and a directional one on the 2-dimensional unit sphere to model r and $\mathbf{v}$ respectively) that leads to an analytical relation between the theoretical diffusion signals and the parameters of the model, as required by the analysis of dMRI data sets.
To circumvent this issue, we express the random variable $\mathbf{w}$ as the sum of two independent random variables, $\mathbf{w} = \mathbf{v} + \mathbf{z}$, where:

• $\mathbf{v}$ follows a **von Mises & Fisher** probability distribution (see Appendix .2) defined on the 2-dimensional sphere of radius $R > 0$ and parametrized by its mean direction $\boldsymbol{\mu}$, with $\|\boldsymbol{\mu}\| = 1$, and its concentration parameter $\kappa \geq 0$. The higher the concentration parameter, the more likely the water molecules are to diffuse along $\boldsymbol{\mu}$; when it is nil, the direction of molecular displacements is uniformly distributed over the sphere; $\boldsymbol{\mu}$ can thus be interpreted as the direction of diffusion, whereas κ can be interpreted as a measure of anisotropy of the diffusion. The von Mises & Fisher probability distribution admits a pdf on the 2-dimensional sphere of radius R. Its expression is given in [44] for $R = 1$ and can easily be extended on the sphere of radius $R > 0$ by affine transformation. For any $\boldsymbol{v} \in \mathbb{R}^3$ such that $\|\boldsymbol{v}\| = R$, we indeed have:

$$f_{\mathbf{v}}(\boldsymbol{v}; \boldsymbol{\mu}, \kappa, R) = \frac{1}{R^3} \frac{\kappa}{4\pi \operatorname{sh} \kappa} \mathrm{e}^{\frac{\kappa}{R} \boldsymbol{\mu}' \boldsymbol{v}} \ . \tag{2}$$

• $\mathbf{z}$ follows a centered **Gaussian** probability distribution defined on $\mathbb{R}^3$ and parametrized by a cylindrically constrained covariance matrix D, akin to the diffusion tensor in the constrained DTI model proposed in [45], completely determined by its condition number (i.e., the ratio of its largest non-zero eigenvalue to its smallest non-zero eigenvalue) set to $\kappa + 1$ and its largest eigenvalue set to R^2 with associated eigenvector set to $\boldsymbol{\mu}$ so that $D = \dfrac{R^2}{\kappa + 1} (I_3 + \kappa \boldsymbol{\mu} \boldsymbol{\mu}')$, where I_3 is the 3×3 identity matrix. If $\kappa \to +\infty$, then $D = R^2 \boldsymbol{\mu} \boldsymbol{\mu}'$ and thus R represents the mean radial displacement along the direction of diffusion $\boldsymbol{\mu}$; if $\kappa \to 0$, then $D = R^2 I_3$ and thus R represents the mean radial displacement along any direction. The centered "cylindrical" Gaussian pdf can be conveniently rewritten using the Sherman-Morrison-Woodbury identity [46] to invert D. For any $\boldsymbol{z} \in \mathbb{R}^3$, we indeed have:

$$f_{\mathbf{z}}(\boldsymbol{z}; \boldsymbol{\mu}, \kappa, R) = \frac{\kappa + 1}{\left(R\sqrt{2\pi}\right)^3} \mathrm{e}^{-\frac{(\kappa+1)\|\boldsymbol{z}\|^2 - \kappa(\boldsymbol{\mu}'\boldsymbol{z})^2}{2R^2}} \ . \tag{3}$$

• $\mathbf{v}$ and $\mathbf{z}$ are statistically independent.

The diffusion pdf amounts to a convolution of the von Mises & Fisher pdf defined on the 2-dimensional sphere of radius R according to Eq.(2) and the Gaussian pdf defined on $\mathbb{R}^3$ according to Eq.(3), and is parametrized by $\boldsymbol{\mu}$ (unit vector), $\kappa \geq 0$ and $R > 0$ (i.e., four parameters). For any $\boldsymbol{w} \in \mathbb{R}^3$, we have (see Appendix .3):

$$\begin{aligned} f_{\mathbf{w}}(\boldsymbol{w}; \boldsymbol{\mu}, \kappa, R) &= c(\kappa, R) \mathrm{e}^{-\frac{1}{2}\left((\kappa+1)w_\perp^2 + w_{/\!/}^2\right)} \\ &\times \int_{-1}^{1} \mathrm{e}^{\frac{\kappa}{2}t^2 + (\kappa + w_{/\!/})t} I_0\left((\kappa+1) w_\perp \sqrt{1-t^2}\right) dt \ , \end{aligned} \tag{4}$$

where $(w_{/\!/}, w_\perp) := R^{-1}\left(\boldsymbol{\mu}'\boldsymbol{w}, \sqrt{\|\boldsymbol{w}\|^2 - (\boldsymbol{\mu}'\boldsymbol{w})^2}\right)$, $c(\kappa, R) := \dfrac{\kappa(\kappa+1)\sqrt{2}}{8\pi^{3/2} R^3 \operatorname{sh}(\kappa)} \mathrm{e}^{-\frac{\kappa+1}{2}}$ and I_0 is the zero-*th* order modified Bessel function [47], with the convention that $\boldsymbol{\mu}'\boldsymbol{w} = \|\boldsymbol{w}\|$ for any $\boldsymbol{w} \in \mathbb{R}^3$ when $\kappa = 0$.

Diffusion model along a specific fiber orientation Let a be the proportion of water molecules in the compartment that diffuse along the direction $+\boldsymbol{\mu}$.

We define the diffusion pdf (i.e., the pdf of the 3-dimensional random variable $\mathbf{y}$) within this compartment as:

$$f_{\mathbf{y}}(\boldsymbol{y};\boldsymbol{\mu},\kappa,R,a) = a \cdot f_{\mathbf{w}}(\boldsymbol{y};\boldsymbol{\mu},\kappa,R) + (1-a) \cdot f_{\mathbf{w}}(\boldsymbol{y};-\boldsymbol{\mu},\kappa,R) \ ,$$

where $f_{\mathbf{w}}$ is given by Eq.(4).
The parameter $a \in [0,1]$ controls the degree of asymmetry of the diffusion pdf. In this work, we adopt a symmetric difffusion pdf obtained assuming equal proportions of water molecules that diffuse along each direction of diffusion. In essence, for a single compartment, we propose the following parametric modeling of the diffusion pdf:

$$f_{\mathbf{y}}(\boldsymbol{y};\boldsymbol{\mu},\kappa,R,a) = \frac{1}{2} \cdot f_{\mathbf{w}}(\boldsymbol{y};\boldsymbol{\mu},\kappa,R) + \frac{1}{2} \cdot f_{\mathbf{w}}(\boldsymbol{y};-\boldsymbol{\mu},\kappa,R) \ , \tag{5}$$

where $f_{\mathbf{w}}$ is given by Eq.(4).

Diffusion features. The random variable $\mathbf{v}$ models exclusively the angular component of the diffusion while the random variable $\mathbf{z}$ mainly models the radial component of the diffusion. Indeed, the shape of the covariance matrix D of the Gaussian probability distribution, with its two smallest eigenvalues being equal, is analogous to a cylinder whose axis lies along the mean direction $\boldsymbol{\mu}$ of the von Mises & Fisher probability distribution. This prevents water molecules from strongly deviating from the direction $\boldsymbol{\mu}$, which makes the largest eigenvalue R^2 of D being a fair approximation of the squared radial displacement.
Within each compartment of each voxel, the **putative fiber orientation** and the **mean radial displacement of water molecules** are naturally identified to $\pm\boldsymbol{\mu}$ and R respectively in our model. The κ parameter completes the description of the diffusion in a compartment by assessing the degree of local anisotropy.
The covariance matrix D involved in our single-compartment model is akin to a diffusion tensor. Its largest and smallest eigenvalues, R^2 and $R^2/(\kappa+1)$ respectively, can thus be interpreted as the **principal and transverse diffusivities**, respectively.
For ease of interpretation by clinicians, we can additionally relate κ and R to the **fractional anisotropy** (FA) and the **mean diffusivity** (MD) [48]. Elementary derivations yield:

$$\mathrm{FA} = \frac{\kappa}{\sqrt{(\kappa+1)^2+2}} \ , \qquad \text{for any } \kappa \geq 0 \ , \tag{6}$$

$$\mathrm{MD} = \left(1+\frac{\kappa}{3}\right)\frac{R^2}{\kappa+1} \ , \qquad \text{for any } \kappa \geq 0 \ , \ R > 0 \ .$$

2.1.2 Multi-compartment Model

Mixture model Due to the low number of parameters of our single-compartment model (4), we can embody it within a multi-compartment model, which can account for more than one fiber orientation within each voxel while keeping the number of parameters reasonably low. This approach was pioneered in [18, 20], using DTI as single-compartment model, and was quite promising. Unfortunately, this model, a.k.a. "multi-tensor" model, requires dMRI data sets acquired on multiple spherical shells [21], which is not compatible with clinical

settings. We thereby propose the same approach using our single-compartment model instead.

Assuming m different fiber orientations within a given voxel, we model the diffusion pdf as a mixture of m pdfs (**fiber compartments**) having the common parametric form given in Eq.(5) with parameters $\{\boldsymbol{\mu}_i, \kappa_i, R_i\}_{i\in[\![1,m]\!]}$. We also include an additional pdf in the mixture to account for isotropic diffusion (**isotropic compartment**). This pdf follows the general form given in Eq.(5) with $\kappa = 0$: in that case, for any $\boldsymbol{w} \in \mathbb{R}^3$, defining $w_R = \|\boldsymbol{w}\|/R$, one can show that:

$$f_{\text{iso}}(\boldsymbol{w}; R) = 2c(0,R)\mathrm{e}^{-\frac{w_R^2}{2}} \frac{\operatorname{sh} w_R}{w_R} \ . \tag{7}$$

Mixture weights We have to associate a weight to each of the $m+1$ pdfs that compose the mixture. We choose to let the weight $w_0 \in [0,1]$ of the isotropic compartment be a free parameter. As the isotropic compartment is explicitly included in the mixture, any fiber compartment with a null κ should vanish from the mixture. Accordingly, the lower a κ, the more down-weighted the associated fiber compartment should be. The weights of the fiber compartments are thus set proportional to their κ value, according to

$$w_i = \frac{(1-w_0)\kappa_i}{\sum_{\ell=1}^m \kappa_\ell} \ , \text{ for any } i \in [\![1,m]\!] \ .$$

Mixture diffusivities Based on the argument that nerve fibers share similar dimensions, the principal and transverse diffusivities are often assumed identical in each compartment [49, 39]. We follow the same lines for the transverse diffusivity but we choose to let each compartment have its own principal diffusivity to robustify the estimation of the associated fiber orientation. For any $i \in [\![1,m]\!]$, we thus have $R_i^2 = (\kappa_i+1)\lambda$, where $\lambda > 0$ is the **common** transverse diffusivity.

The DDI model Our assumptions on the form of the diffusion pdf (Section 2.1.2) along with the assumptions relative to its parametrization (Sections 2.1.2 and 2.1.2) allows us to state our DDI model.

Assuming m putative fiber orientations in the voxel, DDI defines the diffusion pdf as follows:

$$\begin{aligned} f_{\mathbf{w}}\left(\boldsymbol{w}; \{\pm\boldsymbol{\mu}_i, \kappa_i\}_{i\in[\![1,m]\!]}, \lambda, w_0\right) &= w_0 f_{\text{iso}}\left(\boldsymbol{w}; \sqrt{\lambda}\right) \\ &+ \frac{1-w_0}{\sum_{\ell=1}^m \kappa_\ell} \sum_{i=1}^m \kappa_i f_i\left(\boldsymbol{w}; \pm\boldsymbol{\mu}_i, \kappa_i, \sqrt{(\kappa_i+1)\lambda}\right) \ , \end{aligned} \tag{8}$$

where f_{iso} is given by Eq.(7) and f_i is given by Eq.(5), for any $i \in [\![1,m]\!]$.

It is thus parametrized by $3m+2$ parameters (e.g., 5 parameters for the 1-fiber DDI model, 8 parameters for the 2-fiber DDI model), namely:

- the spherical coordinates $(\theta_i, \phi_i) \in [0,\pi] \times [0, 2\pi[$ of the putative fiber orientation $\pm\boldsymbol{\mu}_i$, for any $i \in [\![1,m]\!]$;
- the concentration of water molecules $\kappa_i \geq 0$ around the putative fiber orientation $\pm\boldsymbol{\mu}_i$, for any $i \in [\![1,m]\!]$;
- the transverse diffusivity $\lambda > 0$, common to all compartments;

- the proportion $w_0 \in [0,1]$ of water molecules that are subject to isotropic diffusion.

2.2 Estimation of the DDI Parameters

2.2.1 Analytical expression of the theoretical diffusion signal

An analytical relation between the theoretical diffusion signal $A(b,\boldsymbol{g})$, which depends on the b-value and direction ($\boldsymbol{g}$) of the applied magnetic field gradient, and the parameters of the DDI model can be derived by computing analytically the integral in Eq.(1).

This integral is, by definition, the characteristic function (cf) of the real 3-dimensional random variable $\mathbf{x} = \sqrt{2\,(\Delta - \delta/3)}\mathbf{w}$ (see Section .1 for the definitions), denoted by $\varphi_{\mathbf{x}}$, meaning that Eq.(1) can be written (taking the modulus of each part of the equation):

$$\begin{aligned} \frac{A(b,\boldsymbol{g})}{A(\mathbf{0})} &= \left|\varphi_{\mathbf{x}}\left(\sqrt{\frac{b}{\Delta-\delta/3}}\boldsymbol{g}\right)\right| \\ &= \left|\varphi_{\sqrt{2(\Delta-\delta/3)}\mathbf{w}}\left(\sqrt{\frac{b}{\Delta-\delta/3}}\boldsymbol{g}\right)\right| = \left|\varphi_{\mathbf{w}}\left(\sqrt{2b}\boldsymbol{g}\right)\right| \ . \end{aligned} \tag{9}$$

Assuming that $\mathbf{w}$ follows the DDI model, i.e., that its pdf is given by Eq.(8), $\varphi_{\mathbf{w}}\left(\sqrt{2b}\boldsymbol{g}\right)$ reads:

$$\begin{aligned} \varphi_{\mathbf{w}}\left(\sqrt{2b}\boldsymbol{g};\{\pm\boldsymbol{\mu}_i,\kappa_i\}_{i\in[\![1,m]\!]},\lambda,w_0\right) &= w_0\varphi_{\text{iso}}\left(\sqrt{2b}\boldsymbol{g};\sqrt{\lambda}\right) \\ + \frac{1-w_0}{\sum_{\ell=1}^{m}\kappa_\ell}\sum_{i=1}^{m}\kappa_i\varphi_i\left(\sqrt{2b}\boldsymbol{g};\pm\boldsymbol{\mu}_i,\kappa_i,\sqrt{(\kappa_i+1)\lambda}\right) \ . \end{aligned} \tag{10}$$

As explained in Appendix .2, we have:

$$\varphi_{\text{iso}}\left(\sqrt{2b}\boldsymbol{g};\sqrt{\lambda}\right) = \mathrm{e}^{-b\lambda}\frac{\sin\sqrt{2b\lambda}}{\sqrt{2b\lambda}} \ , \text{ and}$$

$$\begin{aligned} \varphi_i\left(\sqrt{2b}\boldsymbol{g};\pm\boldsymbol{\mu}_i,\kappa_i,\sqrt{(\kappa_i+1)\lambda}\right) &= \mathrm{e}^{-b\lambda\left(1+\kappa_i(\boldsymbol{\mu}_i'\boldsymbol{g})^2\right)} \\ \times\frac{\kappa_i}{\operatorname{sh}\kappa_i}&\begin{cases} \dfrac{\sin\sqrt{2(\kappa_i+1)b\lambda-\kappa_i^2}}{\sqrt{2(\kappa_i+1)b\lambda-\kappa_i^2}} \ , & \sqrt{2b}\boldsymbol{g}\in\Omega_i \ , \\ \dfrac{\alpha_i\operatorname{sh}\alpha_i\cos\beta_i+\beta_i\operatorname{ch}\alpha_i\sin\beta_i}{\alpha_i^2+\beta_i^2} \ , & \sqrt{2b}\boldsymbol{g}\notin\Omega_i \ , \end{cases} \end{aligned}$$

where Ω_i is given by Eq.(15) with $\kappa=\kappa_i$ and $R_i=\sqrt{(\kappa_i+1)\lambda}$, for any $i\in[\![1,m]\!]$, and α_i and β_i are given by Eq.(14), with $\boldsymbol{t}=\sqrt{2b}\boldsymbol{g}$, $\kappa=\kappa_i$ and $R_i=\sqrt{(\kappa_i+1)\lambda}$, for any $i\in[\![1,m]\!]$.

Inserting Eq.(10) into Eq.(9) yields the analytical relationship between the theoretical diffusion signal $A(b,\boldsymbol{g})$ and the parameters $\left\{\{\boldsymbol{\mu}_i,\kappa_i\}_{i\in[\![1,m]\!]},\lambda\right\}$ of the DDI model.

2.2.2 Asymptotic behaviors

Two limiting cases of Eq.(9) and Eq.(10) are quite interesting as they reveal the existing link between our DDI model and other well-known models.

Case $\kappa_i \to 0$ and $\kappa_j/\kappa_i \to 1$, $\forall i,j \in [\![1,m]\!]$ It is the isotropic model; the m fiber compartments are equally weighted and equal to the isotropic compartment. The model thus simplifies to a unique isotropic compartment with unit weight and one can easily show that the theoretical diffusion signal does not depend on the gradient direction but only on the b value and reads:

$$A_{\text{iso}}^{\text{DDI}}(b;\lambda) = A(0)\mathrm{e}^{-b\lambda}\frac{\left|\sin\sqrt{2b\lambda}\right|}{\sqrt{2b\lambda}}\ , \tag{11}$$

which is equal, up to a multiplicative factor, to the expression obtained using the isotropic DTI model [50]: $A_{\text{iso}}^{\text{DTI}}(b;\lambda) = A(0)\mathrm{e}^{-b\lambda}$. In particular, Eq.(11) reduces to the isotropic DTI model for low b values as $\sin(x)/x \xrightarrow{x\to 0} 1$. On the other hand, we suggest a slight departure from the isotropic DTI model for high b values as it has been shown that the Gaussian model is inadequate [51].

Case $\kappa_i \to +\infty$, $0 < R_i^2 = (\kappa_i+1)\lambda < +\infty$ and $\kappa_j/\kappa_i \to 1$, $\forall i,j \in [\![1,m]\!]$ In this case, the transverse diffusivity goes to zero, the m fiber compartments are equally weighted and the principal diffusivities R_i^2 all converge to the same finite value R^2; one can then easily show that the theoretical diffusion signal reads:

$$A_{\infty}^{\text{DDI}}\left(b,\boldsymbol{g};\{\pm\boldsymbol{\mu}_i\}_{i\in[\![1,m]\!]},R\right) = A(\mathbf{0})\left(w_0 + \frac{1-w_0}{m}\sum_{i=1}^{m}\mathrm{e}^{-bR^2(\boldsymbol{\mu}_i'\boldsymbol{g})^2}\right)$$

This limiting case of our model is very similar to the model proposed in [19] using Watson distributions, which is a constrained multi-tensor model where the tensors have a unique non-zero eigenvalue and the compartments are equally weighted. The only difference relies on a possible non-zero proportion w_0 of water molecules that are subject to isotropic diffusion (and thus do not contribute in the attenuation of the theoretical diffusion signal since the transverse diffusivity is nil) which our asymptotic model include.

2.2.3 Estimation from noisy diffusion signals

Description of a dMRI data set. In its most general form, a dMRI data set is composed of $n_g \times n_b$ raw diffusion signals S_{jk}, $j \in [\![1,n_g]\!]$, $k \in [\![1,n_b]\!]$, acquired for n_g different encoding directions $\{\boldsymbol{g}_j\}_{j\in[\![1,n_g]\!]}$ and n_b different encoding b-values $\{b_k\}_{k\in[\![1,n_b]\!]}$. Each raw diffusion signal is corrupted by Rician noise [6], as $S_{jk} \sim \text{Rice}\left(A_{jk},\sigma_k\right)$, where $\sigma_k \geq 0$ is the standard deviation of the noise which depends on the b-value, and A_{jk} is the corresponding theoretical diffusion signal which is analytically related to the parameters of the DDI model.

Handling the Rician noise. Because of the Rician noise, in general, the mean of a raw diffusion signal S_{jk} does not match the corresponding theoretical diffusion signal A_{jk}. For moderate (typically greater than 3) signal-to-noise ratio (SNR), defined as $\text{SNR}_{jk} = A_{jk}/\sigma_k$, the following Gaussian approximation

of the Rician noise holds [6]: $S_{jk} \sim \mathrm{N}\left(\sqrt{A_{jk}^2 + \sigma_k^2}, \sigma_k^2\right)$. This approximation however requires σ_k to be known which is not the case in practice. We instead use an estimate of it computed according to [52]. For low SNRs, we first filter the images with the Rician-adapted Non-Local Means filter [52], which has been shown to efficiently denoise such images while preserving fine anatomical structures. In particular, this filter has also been shown to preserve the angular resolution of QBI [53].

Minimization problem. Assuming that the Gaussian approximation of the Rician noise holds for all b-values and has known variance, a least squares (LS) fitting is adequate and the estimation of the DDI parameters can be performed by minimizing the following criterion:

$$J\left(\{\pm\boldsymbol{\mu}_i, \kappa_i\}_{i\in[\![1,m]\!]}, \lambda; \{S_{jk}\}\right) = \sum_{j=1}^{n_g}\sum_{k=1}^{n_b}\left(\frac{S_{jk} - \sqrt{A_{jk}^2\left(\{\pm\boldsymbol{\mu}_i, \kappa_i\}_{i\in[\![1,m]\!]}, \lambda\right) + \sigma_k^2}}{\sigma_k}\right)^2 .$$

The optimization of the cost function J is performed using the derivative-free new unconstrained optimization algorithm (NEWUOA) [54]. Each parameter of the DDI model is thus transformed into an unconstrained parameter using the general transformation $p = p_{\min} + p_{\max}\left(\sin(p^\star) + 1\right)/2$, where p is any parameter of the DDI model and $p^\star$ the associated unconstrained parameter. The value of $p_{\min}$ was set to 0 for all the parameters. The value of $p_{\max}$ was set to π for the parameters $\{\theta_i\}_{i\in[\![1,m]\!]}$ and $\{\phi_i\}_{i\in[\![1,m]\!]}$ (we limit the search to the hemisphere since we are dealing with orientations), 50 for $\{\kappa_i\}_{i\in[\![1,m]\!]}$ and 0.003 for λ.

2.2.4 Model Selection

The DDI model also requires a model selection step since the number m of fiber orientations in a voxel is not *a priori* known. In practice:

- We choose a maximum M of putative fiber orientations within a voxel.
- We perform the estimation of the DDI parameters for $m \in \{0, 1, 2, \ldots, M\}$.
- We select the model with minimum corrected Akaike's Information Criterion (AICc) [55]:

$$\mathrm{AICc}(m) = \chi^2 + 6m + 4 + \frac{6(3m+2)(m+1)}{n_b n_g - 3m - 3} ,$$

where χ^2 is the minimum value of the cost function J. In essence, this criterion is a modified version of the original AIC [56] which accounts for the over-fitting problem that occurs when the AIC is computed from data sets with a too small sample size $n_b n_g$.

3 Results

3.1 Simulation study

3.1.1 Goals

Results on simulated data are performed at the voxel level and have different scopes:

- Analyzing the angular error committed on the estimates of the fiber orientation(s) via a cone-of-uncertainty analysis [57];
- Determining the angular resolution of the 2-fiber DDI model.

No evalution is made in this study on the κ and λ values that are provided by the DDI model. We will tackle this issue in a future work. Instead, we focus here on assessing the capability of the DDI model to accurately estimate fiber orientations.

3.1.2 Generation of the simulated data sets

The simulation study is performed in a unique voxel and with a unique b value of 1500s/mm^2 which is an upper bound of the typical b values used in clinics.

To generate the simulated data sets, we use a spherical deconvolution method proposed in [40] referred to as BV in our study. To simulate multiple fiber orientations, they assume that the fODF is a sum of equally-weighted delta functions. They perform its convolution with the kernel proposed in [58], which models restricted diffusion within a cylindrical fiber of radius $\rho = 5\mu$m and length L= 5mm. There are three reasons to such a choice: (i) they implemented this generator of diffusion signals on-line, as part of the fanDTasia toolbox[3], (ii) this generator has been used in more than 20 papers and (iii) the spherical deconvolution in its discrete version is close to multi-compartment models.

We simulated both the single-fiber and two-fiber cases with, for each of them, $\mathrm{N}_a = 5$ sets of respectively 15, 30, 41, 64 and 200 encoding gradient directions uniformly distributed on the hemisphere. For a given case (single or two-fiber) and a given set of encoding gradient directions, we generated several configurations of the fiber orientations and we corrupted each data set with $\mathrm{N}_s = 12$ increasing noise levels (SNR $= +\infty, 30, 25, 20, 16, 13, 10, 7, 5, 3, 2, 1$).

The configurations of fiber orientations were defined as follows. For each case (single or two-fiber), the first fiber was set to $\mathrm{N}_{d_1} = 5$ different values (θ, ϕ), with $\theta = 90$ and $\phi = 0, 30, 45, 60, 90$ (in degree). For the two-fiber case, the second fiber was set to $\mathrm{N}_{d_2} = 25$ different values $(\theta, \phi + \Delta\phi)$ for each value of the first fiber, with $\Delta\phi$ going from 90 to 60 degrees with a step of 10 degrees, from 60 to 30 degrees with a step of 5 degrees and from 30 to 0 degree with a step of 2 degrees.

We obtained $\mathrm{N}_a\mathrm{N}_s(\mathrm{N}_{d_2} + 1)\mathrm{N}_{d_1} = 7800$ data sets in a given voxel, each one of them characterized by (i) a number of fiber orientations, (ii) a number of encoding directions, (iii) an SNR value, (iv) an orientation of the first fiber and, for two-fiber cases, (v) the angle between the two fibers. Finally, we resampled each data sets 100 times to allow for statistical assessment on the estimated parameters.

[3] http://www.cise.ufl.edu/ abarmpou/lab/DWMRI.simulator.php

3.1.3 Analysis

Cone-of-uncertainty analysis The cone-of-uncertainty analysis [57] consists in displaying the 95% confidence intervals of the estimated fiber orientations using a cone shape with axis that lies on the mean fiber orientation and angle equal to the 95% confidence angle between an estimated orientation and its corresponding ground truth.

The computation of this confidence angle is performed via the percentile method: for each data set, we compute the 100 angles between each estimated fiber orientation and its corresponding ground truth; we then sort these angles and take the $95th$ as the 95% confidence angle.

Figure 1 shows the cones of uncertainty of some data sets. In details, all the data sets represented are two-fiber cases with a first fiber orientation at $\pm(\sqrt{2}/2, \sqrt{2}/2, 0)$ simulated from 30 encoding gradient directions and a single b value of 1500s/mm^2 (typical clinical situation). From the top to the bottom, the second fiber orientation is moved aside the first one with increasing angle from 0 degrees to 90 degrees as described in Section 3.1.2. From the left to the right, SNR is increased from 1 to $+\infty$ as described in Section 3.1.2.

The idea behind the cone-of-uncertainty analysis is that two estimated fiber orientations become indistinguishable when the confidence cones strongly overlap. In Fig.1, we see that the closer the fiber orientations, the harder it is to distinguish them using DDI which makes sense. We also note that the more important the noise, the larger the cones become, which indicates a non accurate estimation of the fiber orientations.

A way to read a cone-of-uncertainty analysis is to select a noise level and step the angle between the two fiber orientations down, starting from its largest (i.e., 90 degrees in our case), until the two cones strongly overlap. This gives a qualitative measure of the angular resolution of the method for this particular noise level and for this number of encoding gradient directions: for example, with 30 encoding gradient directions and an SNR of 10, Fig.1 shows that the angular resolution of DDI is about 30 degrees. It is however possible to quantify it and this is the object of the next paragraph.

Angular resolution of the two-fiber DDI method The *angular resolution* is the minimum detectable angle between two different fiber orientations. To estimate it, we do not perform any model selection and we use the data sets simulated by BV.

The simulated data sets with ground truth angle of zero degrees between the two fiber orientations are single fiber cases. Their 95% confidence angle is thus a fair approximation of the angular resolution since any voxel in which crossing fibers are estimated with an angle that drops below this value has a significant probability to contain only one single fiber.

For each data set, we thus compute the confidence angle between the two estimated directions using the percentile method. In order to minimize the effect of the sensitivity of the initialization of the NEWUAO algorithm on the estimation of the angular resolution, we take the minimum 95% confidence angle over the different fiber configurations that we simulated.

Following these main steps, we were able to compute an estimated angular resolution of DDI for each number of encoding gradient directions and for each noise level. The results are reported in Table 2.

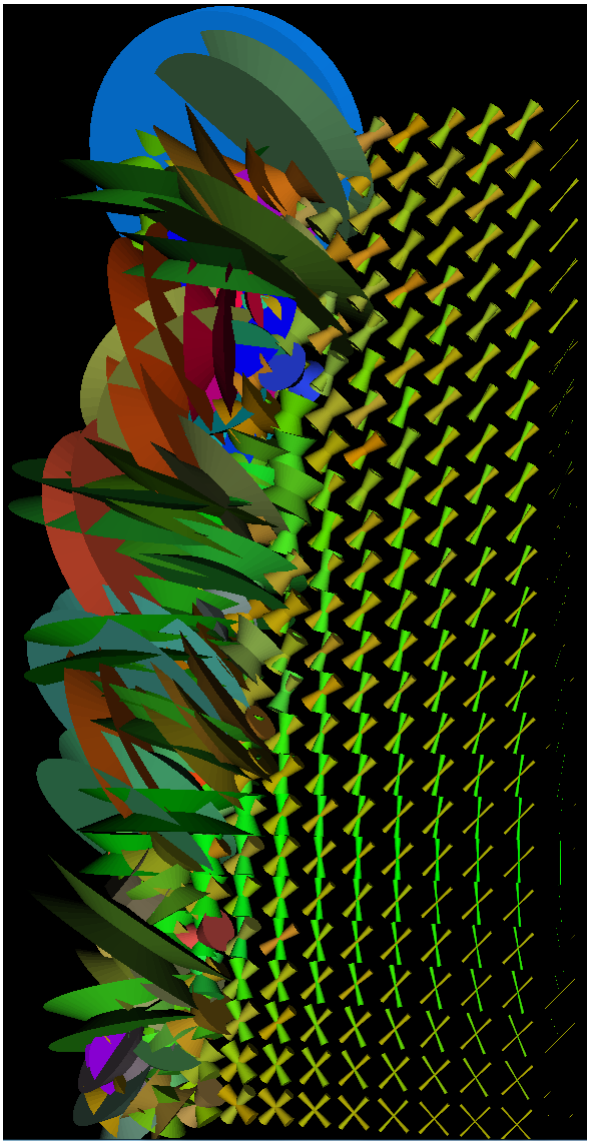

Figure 1: Cones of uncertainty of the estimated fiber orientations from diffusion signals simulated with 30 encoding gradient directions, a fixed first fiber at $\pm(\sqrt{2}/2, \sqrt{2}/2, 0)$ and various SNRs and second fiber orientation.

Table 2 shows that the angular resolution of DDI improves as SNR increases and as the number of encoding gradient directions increases. It is interesting to observe that, even in absence of noise, the model cannot distinguish two fiber orientations that are separated by an angle smaller than 1.7 degrees. Another interesting fact is that, for low SNRs, increasing drastically the number of encoding gradient directions does not seem to improve significantly the angular resolution obtained with few encoding directions. Last, we can conclude from

Table 2: Angular resolution (in degrees) of the DDI method for various SNRs and number of encoding gradient directions. The estimation is performed via LS fitting without any correction of the mean to account for the Rician noise.

	Number of encoding gradient directions				
SNR	15	30	41	64	200
1	81.6935	82.3828	75.6493	82.1945	75.8231
2	75.4626	77.5608	79.8586	72.5307	72.5959
3	70.6784	67.9172	64.5632	50.9299	51.2468
5	61.8446	55.2778	47.3007	42.9176	26.7046
7	50.1703	42.9719	34.1863	27.6380	21.9324
10	43.9055	29.1703	25.8254	23.0921	17.1725
13	31.2371	24.3971	22.7992	19.8612	14.5524
16	29.3666	22.7685	21.1694	18.2829	13.0752
20	25.8926	20.5858	18.2044	15.6704	11.5458
25	21.9832	17.9714	15.9505	13.7777	10.0341
30	20.5242	16.4157	13.4003	12.9833	8.9419
inf	1.6646	1.3938	0.5617	0.2857	0.1161

Table 2 that, for standard clinical dMRI data sets (SNR between 7 and 10, 30 encoding gradient directions), the angular resolution of DDI is about 35 degrees.

3.2 Real data experiments

Acquisitions. We perform a dMRI sequence on a healthy subject using a 3T Siemens MRI scanner. The sequence consisted of a single encoding b value of 800s/mm^2 and 15 encoding gradient directions. The aim of this acquisition is to show an example of visualization of the DDI parameters, estimated from a poor quality clinical acquisition.

Preprocessing. With such clinical conditions, the resulting diffusion-weighted images were very noisy. We thus apply the Rician-adapted Non-Local Means filter [52] to them before proceeding with the estimation of the DDI parameters. This denoising step allows us to consider that the mean of the denoised raw diffusion signal matches its theoretical value and, thus, we perform the estimation with a classical LS fitting of the model on the denoised raw diffusion signals.

Visualization of the DDI parameters. We propose the cone glyph to visualize the DDI parameters. In each voxel of the image, we display as many cones as estimated fiber orientations. The axis of each cone lies on its corresponding estimated fiber orientation $\pm\boldsymbol{\mu}$. The radius is inversely proportional to the concentration κ of water molecules around the fiber orientation and the height of the cone is proportional to the mean squared radial displacement $(\kappa+1)\lambda$, where λ is akin to the transverse diffusivity. A line thus represent a trustworthy estimated fiber orientation while a disk indicates the contrary. As an example, Fig.2 shows an axial slice of the brain of our healthy subject...

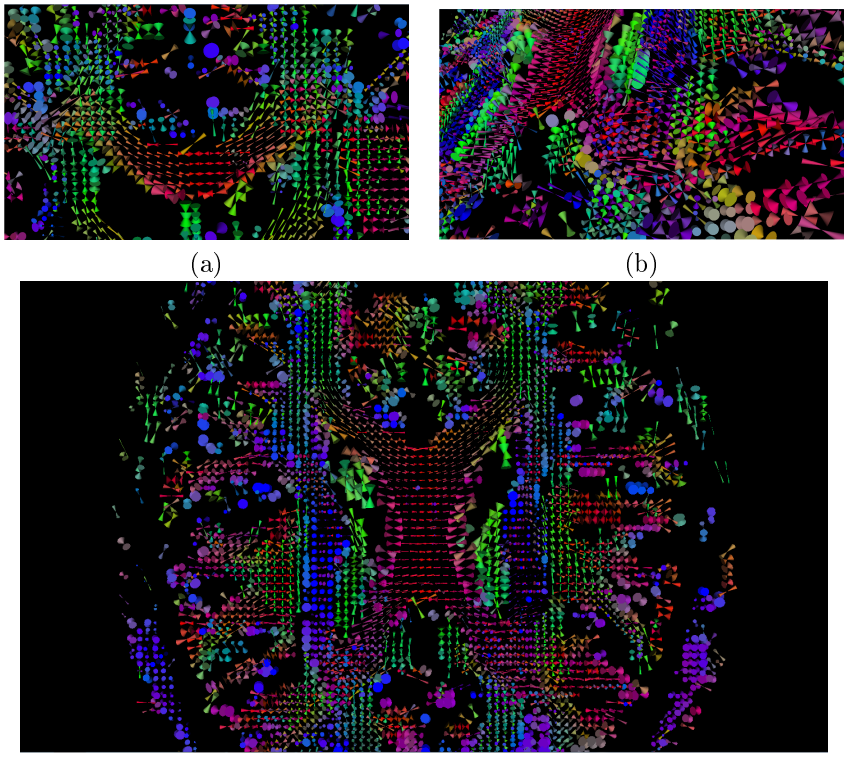

(a) (b)

(c)

Figure 2: Visualization of the DDI parameters using cone glyphs on an axial slice of a subject's brain. The parameters are estimated from poor quality diffusion signals ($b = 800\text{s/mm}^2$, 15 encoding gradient directions). Figure (a) shows slice 42 where crossing fibers are detected at the extremities of the corpus callosum while Figure (b) and (c) show slice 48 where crossing fibers are detected, notably on the cortico-spinal tract.

4 Discussion and Conclusion

4.1 Theoretical aspects

In this paper, we proposed Diffusion Directions Imaging, a new method for the analysis of dMRI data sets. At the heart of this method lies a careful modeling of the random displacements of the water molecules diffusing along one of the two directions of a given fiber. We indeed conveniently separate the angular and radial components of the diffusion. Assuming that water molecules along a given fiber diffuse in equal proportions in both directions yields our single-compartment model of the diffusion pdf. Finally, we account for multiple fiber orientations by encompassing the single-compartment model within a multi-compartment model.

On the same line as DTI, we thus propose a parametric modeling of the diffusion pdf and we also derive the analytical relation between its parameters and the theoretical diffusion signals. For m putative fiber orientations in a given

voxel, only $3m+2$ parameters need to be estimated to get an estimation of the diffusion pdf (e.g., only 8 parameters to estimate a fiber crossing).

In the single-compartment model, we choose to symmetrize the diffusion pdf by assuming equal proportions of water molecules diffusing in the two directions of the fiber ($a = 1/2$) which is an assumption that almost any state-of-the-art method claims. However, it has been shown in [17] that, at low b values (typically less than 1500s/mm^2), the theoretical diffusion signals resulting from crossing fibers and Y-shaped mixed fibers are indistinguishable but that they become more and more different as the b value increases. The model of the diffusion pdf in DDI is easily asymmetrizable (taking $a \neq 1/2$ is sufficient) and thus, as a perspective, we try to evaluate the benefits of this property when the b value is higher.

The model selection is also very simple and we did not study its performances. This will be the object of a future work.

4.2 Practical aspects

We focused on evaluate the ability of DDI to accurately estimate fiber orientations. To that end, we performed a cone-of-uncertainty analysis which allowed for a qualitative measure of the angular resolution of the method. Next, we computed a quantitative measure of it which confirmed the qualitative results. With standard clinical acquisitions, we showed that the angular resolution of the two-fiber DDI is about 35 degrees. This result seems to be very encouraging although a deep comparison with some state-of-the art methods needs to be carried out.

As another perspective, we would like to perform similar studies to assess the accuracy of the other parameters that DDI provides, namely κ (concentration of water molecules around a given orientation), λ (akin to the transverse diffusivity) and w_0 (proportion of water molecules subject to isotropic diffusion).

Moreover, the simulation study revealed that the minimization of the criterion for the estimation of the DDI parameters is very sensitive to the initialization. Whether it is a limitation of the model or a limitation of the NEWUOA optimization algorithm or a combination of these two is still an open issue that we need to address.

.1 Definitions from probability theory

Let us recall some probability theory basics that are required in Appendix .2.

- Given two measurable spaces $(E_1, \mathscr{F}_1)$ and $(E_2, \mathscr{F}_2)$, a measurable function $h : E_1 \to E_2$ and a measure $\rho : \mathscr{F}_1 \to [0, +\infty]$, the **pushforward measure** $h \star \rho : \mathscr{F}_2 \to [0, +\infty]$ of ρ induced by h is defined as $(h \star \rho)(B) = \rho\left(h^{-1}(B)\right)$, for any $B \in \mathscr{F}_2$;
- a real p-dimensional **random variable** $\mathbf{x}$ is a measurable function from the probability space $(\Lambda, \mathscr{F}, P)$ to the measurable space $(\mathbb{R}^p, \mathscr{B}_p)$, where $\mathscr{B}_p$ is the Borel σ-algebra of $\mathbb{R}^p$;
- the **probability distribution** of the real p-dimensional random variable $\mathbf{x}$ is the pushforward measure of P induced by $\mathbf{x}$;

• the **characteristic function** $\varphi_{\mathbf{x}} : \mathbb{R}^p \to \mathbb{C}$ of the real p-dimensional random variable $\mathbf{x}$ reads

$$\begin{aligned}\varphi_{\mathbf{x}}(\boldsymbol{t}) &= \int_{\mathbb{R}^p} \mathrm{e}^{i\boldsymbol{t}'\boldsymbol{x}} \mathrm{d}(\mathbf{x} \star P)(\boldsymbol{x}) = \int_{\mathbb{R}^p} \mathrm{e}^{i\boldsymbol{t}'\boldsymbol{x}} \mathrm{d}P(\mathbf{x}^{-1}(\boldsymbol{x})) \\ &= \int_{\Lambda} \mathrm{e}^{i\boldsymbol{t}'\mathbf{x}(\omega)} \mathrm{d}P(\omega) \ , \text{ for any } \boldsymbol{t} \in \mathbb{R}^p \ .\end{aligned}$$

• the **probability density function** $f_{\mathbf{x}} : \mathbb{R}^p \to [0, +\infty]$ of the real p-dimensional random variable $\mathbf{x}$ is the Radon-Nikodym derivative of its probability distribution.

Note that the cf of the real p-dimensional random variable $\mathbf{x}$ always exists whereas its pdf exists if and only if the probability distribution of $\mathbf{x}$ is absolutely continuous wrt the Lebesgue measure. In the latter case, the cf and the pdf are related by $\varphi_{\mathbf{x}}(\boldsymbol{t}) = \displaystyle\int_{\mathbb{R}^p} \mathrm{e}^{i\boldsymbol{t}'\boldsymbol{x}} f_{\mathbf{x}}(\boldsymbol{x}) \mathrm{d}\boldsymbol{x}$, for any $\boldsymbol{t} \in \mathbb{R}^p$.

.2 The von Mises & Fisher probability distribution

It is a 4-parameter probability distribution. Here is the list of the notations used throughout this section:

• $A_2 = [0, \pi] \times [0, 2\pi[$ is the 2-dimensional space of spherical coordinates; equipped with its corresponding Borel σ-algebra $\mathscr{B}_{A_2}$, it is a measurable space;

• $(\theta_0, \phi_0, \kappa, R) \in A_2 \times [0, +\infty] \times]0, +\infty]$ are the parameters of the von Mises & Fisher probability distribution $F_{\theta_0, \phi_0, \kappa, R}$;

• Denoting $\boldsymbol{\mu} = (\sin\theta_0 \cos\phi_0, \sin\theta_0 \sin\phi_0, \cos\theta_0)'$, the von Mises & Fisher distribution can also be denoted by $F_{\boldsymbol{\mu}, \kappa, R}$;

• $\nu_{\boldsymbol{\mu}, \kappa} : \mathscr{B}_{A_2} \to [0, +\infty]$ is the von Mises & Fisher measure on the 2-dimensional unit sphere whose density wrt the Lebesgue measure reads:

$$\begin{aligned}\mathrm{d}\nu_{\boldsymbol{\mu}, \kappa}(\theta, \phi) = \frac{\kappa \sin\theta}{4\pi \operatorname{sh}\kappa} \exp\{\kappa (\mu_1 \sin\theta\cos\phi \\ + \mu_2 \sin\theta \sin\phi + \mu_3 \cos\theta)\} \, \mathrm{d}\theta \mathrm{d}\phi \ ,\end{aligned} \tag{12}$$

for any $(\theta, \phi) \in A_2$ so that $(A_2, \mathscr{B}_{A_2}, \nu_{\boldsymbol{\mu}, \kappa})$ is a probability space;

• T_R is the real 3-dimensional random variable from $(A_2, \mathscr{B}_{A_2}, \nu_{\boldsymbol{\mu}, \kappa})$ to $\left(\mathbb{R}^3, \mathscr{B}_3\right)$ such that

$$T_R(\theta, \phi) = (R\sin\theta\cos\phi, R\sin\theta\sin\phi, R\cos\theta)' \ , \tag{13}$$

for any $(\theta, \phi) \in A_2$.

Definition: The von Mises & Fisher probability distribution in $\mathbb{R}^3$ is the pushforward measure $F_{\boldsymbol{\mu}, \kappa, R}$ of $\nu_{\boldsymbol{\mu}, \kappa}$ induced by T_R; $\boldsymbol{\mu}$ (unit vector) is the *mean direction*, $\kappa \geq 0$ is the *concentration parameter* which controls the dispersion of the probability distribution around the mean direction $\boldsymbol{\mu}$ and $R > 0$ is the radius of the sphere on which the probability distribution has positive value.

Characteristic function: Let $\mathbf{v}$ be a real 3-dimensional random variable following the von Mises & Fisher probability distribution $F_{\boldsymbol{\mu}, \kappa, R}$. Then, for any $\boldsymbol{t} \in \mathbb{R}^3$, its characteristic function is

$$\varphi_{\mathbf{v}}(\boldsymbol{t}; \boldsymbol{\mu}, \kappa, R) = \int_{A_2} \mathrm{e}^{i\boldsymbol{t}' T_R(\theta, \phi)} \mathrm{d}\nu_{\boldsymbol{\mu}, \kappa}(\theta, \phi) \ ,$$

which, combined with Eq.(12), becomes

$$\varphi_{\mathbf{v}}(\boldsymbol{t};\boldsymbol{\mu},\kappa,R) = \frac{\kappa}{4\pi\,\mathrm{sh}\,\kappa}\int_{A_2} \mathrm{e}^{(iR\boldsymbol{t}+\kappa\boldsymbol{\mu})'T_1(\theta,\phi)}\sin\theta\mathrm{d}\theta\mathrm{d}\phi\ .$$

The derivation of this integral is carried out in [59] for the case $R = 1$. It is straightforward to generalize the expression for any $R > 0$:

$$\varphi_{\mathbf{v}}(\boldsymbol{t};\boldsymbol{\mu},\kappa,R) = \frac{\kappa}{\mathrm{sh}\,\kappa}\sum_{n=0}^{+\infty}\frac{z^n}{(2n+1)!}\ ,\forall \boldsymbol{t}\in\mathbb{R}^3\ ,$$

with $z = z(\boldsymbol{t};\boldsymbol{\mu},\kappa,R) = \kappa^2 - R^2\|\boldsymbol{t}\|^2 + 2i\kappa R\boldsymbol{\mu}'\boldsymbol{t}$.
This expression can be simplified by introducing:

$$\begin{aligned}
\alpha &= \alpha(\boldsymbol{t};\boldsymbol{\mu},\kappa,R) = \sqrt{\frac{\mathrm{Re}\ z + |z|}{2}}\ ,\\
\beta &= \beta(\boldsymbol{t};\boldsymbol{\mu},\kappa,R) = \frac{\mathrm{Im}\ z}{\sqrt{2\,(\mathrm{Re}\ z + |z|)}}\ ,\\
\Omega &= \left\{\boldsymbol{t}\in\mathbb{R}^3 \text{ s.t. } \|\boldsymbol{t}\| \geq \kappa/R \text{ and } \boldsymbol{t}\perp\boldsymbol{\mu}\right\}\ .
\end{aligned} \tag{14}$$

Note the α and β are well-defined only when $\mathrm{Re}\,(z) + |z| > 0$.
This leads to:

$$\varphi_{\mathbf{v}}(\boldsymbol{t};\boldsymbol{\mu},\kappa,R) = \begin{cases} \dfrac{\kappa}{\mathrm{sh}\,\kappa}\dfrac{\sin\sqrt{R^2\|\boldsymbol{t}\|^2-\kappa^2}}{\sqrt{R^2\|\boldsymbol{t}\|^2-\kappa^2}}\ ,\ \boldsymbol{t}\in\Omega\ ,\\ \dfrac{\kappa}{\mathrm{sh}\,\kappa}\dfrac{\mathrm{sh}\,(\alpha+i\beta)}{\alpha+i\beta}\ ,\ \boldsymbol{t}\notin\Omega\ . \end{cases} \tag{15}$$

Remarks. When $\kappa = 0$, the von Mises & Fisher probability distribution coincides with the uniform probability distribution on the 2-dimensional sphere of radius R.
Besides, the von Mises & Fisher probability distribution is not absolutely continuous wrt the Lebesgue measure in $\mathbb{R}^3$ as, for example, A_2 has null Lebesgue measure while $F_{\boldsymbol{\mu},\kappa,R}(A_2) = 1$. Therefore, it does not admit a pdf on $\mathbb{R}^3$.

.3 Independent sum of a von Mises & Fisher variable and a Gaussian variable

Let $\mathbf{w}$ be the independent sum of a von Mises & Fisher random variable $\mathbf{v}$ defined on the 2-dimensional sphere of radius $R > 0$ with pdf given by Eq.(2) and a Gaussian random variable $\mathbf{z}$ defined on $\mathbb{R}^3$ with pdf given by Eq.(3). The random variable $\mathbf{w}$ admits both a cf and a pdf. For any $\boldsymbol{t}\in\mathbb{R}^3$, the former is given by:

$$\varphi_{\mathbf{w}}(\boldsymbol{t};\boldsymbol{\mu},\kappa,R) = \varphi_{\mathbf{v}}(\boldsymbol{t};\boldsymbol{\mu},\kappa,R)\varphi_{\mathbf{z}}(\boldsymbol{t};\boldsymbol{\mu},\kappa,R)\ ,$$

where $\varphi_{\mathbf{v}}(\boldsymbol{t};\boldsymbol{\mu},\kappa,R)$ is given by Eq.(15) and $\varphi_{\mathbf{z}}(\boldsymbol{t};\boldsymbol{\mu},\kappa,R) = \mathrm{e}^{-\frac{R^2}{2(\kappa+1)}\left(\|\boldsymbol{t}\|^2+\kappa(\boldsymbol{\mu}'\boldsymbol{t})^2\right)}$, and, for any $\boldsymbol{w}\in\mathbb{R}^3$, the latter is given by:

$$\begin{aligned}
f_{\mathbf{w}}(\boldsymbol{w};\boldsymbol{\mu},\kappa,R) &= c(\kappa,R)\mathrm{e}^{-\frac{1}{2}\left((\kappa+1)w_\perp^2+w_{/\!/}^2\right)}\\
&\times\int_{-1}^{1}\mathrm{e}^{\frac{\kappa}{2}t^2+(\kappa+w_{/\!/})t}I_0\left((\kappa+1)w_\perp\sqrt{1-t^2}\right)dt\ ,
\end{aligned}$$

where $(w_{/\!/}, w_\perp) := R^{-1}\left(\boldsymbol{\mu}'\boldsymbol{w}, \sqrt{\|\boldsymbol{w}\|^2 - (\boldsymbol{\mu}'\boldsymbol{w})^2}\right)$, $c(\kappa, R) := \dfrac{\kappa(\kappa+1)\sqrt{2}}{8\pi^{3/2}R^3\,\mathrm{sh}\,(\kappa)}\mathrm{e}^{-\frac{\kappa+1}{2}}$ and I_0 is the zero-*th* order modified Bessel function [47], with the convention that $\boldsymbol{\mu}'\boldsymbol{w} = \|\boldsymbol{w}\|$ for any $\boldsymbol{w} \in \mathbb{R}^3$ when $\kappa = 0$.

Proof:

Let $F_{\boldsymbol{\mu},\kappa,R}$, $G_{\boldsymbol{\mu},\kappa,R}$ and $H_{\boldsymbol{\mu},\kappa,R}$ be the probability distributions of the real 3-dimensional random variables $\mathbf{v}$, $\mathbf{z}$ and $\mathbf{w}$ respectively. The statistical independence of the random variables $\mathbf{v}$ and $\mathbf{z}$ implies that:

- the characteristic function of $\mathbf{w}$ reads $\varphi_{\mathbf{w}} = \varphi_{\mathbf{v}+\mathbf{z}} = \varphi_{\mathbf{v}}\varphi_{\mathbf{z}}$; using the expression of the cf of the Gaussian random variable [60] ends the proof for $\varphi_{\mathbf{w}}$;
- the density of $H_{\boldsymbol{\mu},\kappa,R}$ wrt $G_{\boldsymbol{\mu},\kappa,R}$ reads

$$\mathrm{d}H_{\boldsymbol{\mu},\kappa,R}(\boldsymbol{w}) = \int_{\mathbb{R}^3} \mathrm{d}G_{\boldsymbol{\mu},\kappa,R}(\boldsymbol{w}-\boldsymbol{v})\mathrm{d}F_{\boldsymbol{\mu},\kappa,R}(\boldsymbol{v}) \ ,$$

for any $\boldsymbol{w} \in \mathbb{R}^3$; now, $G_{\boldsymbol{\mu},\kappa,R}$ is absolutely continuous wrt the Lebesgue measure, so does $H_{\boldsymbol{\mu},\kappa,R}$. The pdf of $\mathbf{w}$ thereby exists and is given, for any $\boldsymbol{w} \in \mathbb{R}^3$, by

$$f_{\mathbf{w}}(\boldsymbol{w};\boldsymbol{\mu},\kappa,R) = \int_{\mathbb{R}^3} f_{\mathbf{z}}(\boldsymbol{w}-\boldsymbol{v};\boldsymbol{\mu},\kappa,R)\mathrm{d}F_{\boldsymbol{\mu},\kappa,R}(\boldsymbol{v}) \ .$$

Since $F_{\boldsymbol{\mu},\kappa,R}$ is a von Mises & Fisher probability distribution, it is the push-forward measure of $\nu_{\boldsymbol{\mu},\kappa}$ defined in Eq.(12) induced by the random variable T_R defined in Eq.(13). We thus have:

$$\mathrm{d}F_{\boldsymbol{\mu},\kappa,R}(\boldsymbol{v}) = \mathrm{d}\nu_{\boldsymbol{\mu},\kappa}\left(T_R^{-1}(\boldsymbol{v})\right) \ ,\forall \boldsymbol{v} \in \mathbb{R}^3 \ . \tag{16}$$

Combining Eq.(3), Eq.(12) and Eq.(16), we obtain after some simplifications:

$$\begin{aligned} f_{\mathbf{w}}(\boldsymbol{w};\boldsymbol{\mu},\kappa,R) = \frac{c(\kappa,R)}{2\pi}\mathrm{e}^{-\frac{1}{2}\left((\kappa+1)w_\perp^2 + w_{/\!/}^2\right)} \\ \times Q(\boldsymbol{w};\boldsymbol{\mu},\kappa,R) \ , \end{aligned} \tag{17}$$

where $Q : \mathbb{R}^3 \to \mathbb{R}$ is defined as follows:

$$\begin{aligned} Q(\boldsymbol{w};\boldsymbol{\mu},\kappa,R) := \int_{A_2} \mathrm{e}^{\frac{\kappa}{2}\left(\boldsymbol{\mu}'T_1(\theta,\phi)\right)^2}\mathrm{e}^{\kappa\left(1-\frac{\boldsymbol{\mu}'\boldsymbol{w}}{R}\right)\boldsymbol{\mu}'T_1(\theta,\phi)} \\ \times \mathrm{e}^{\frac{\kappa+1}{R}\boldsymbol{w}'T_1(\theta,\phi)}\sin\theta\mathrm{d}\theta\mathrm{d}\phi \ . \end{aligned}$$

Let P be the unitary matrix that rotates $\boldsymbol{\mu}$ to $\boldsymbol{e}_3 = (0,0,1)'$, i.e., $P\boldsymbol{\mu} = \boldsymbol{e}_3$. Defining $\boldsymbol{w}^\star = P\boldsymbol{w}$, we have

$$\begin{aligned} Q(\boldsymbol{w};\boldsymbol{\mu},\kappa,R) &= \int_{A_2} \mathrm{e}^{\frac{\kappa}{2}\cos^2\theta + \kappa\left(1-\frac{\boldsymbol{\mu}'\boldsymbol{w}}{R}\right)\cos\theta} \\ &\times \mathrm{e}^{\frac{\kappa+1}{R}\left(w_1^\star\sin\theta\cos\phi + w_2^\star\sin\theta\sin\phi + w_3^\star\cos\theta\right)}\sin\theta\mathrm{d}\theta\mathrm{d}\phi \ , \\ &= \int_0^\pi \mathrm{e}^{\frac{\kappa}{2}\cos^2\theta + \kappa\left(1-\frac{\boldsymbol{\mu}'\boldsymbol{w}}{R}\right)\cos\theta}h(\boldsymbol{w}^\star,\theta)\sin\theta\mathrm{d}\theta \ , \end{aligned} \tag{18}$$

where $h(\boldsymbol{w}^\star,\theta) := \displaystyle\int_{\phi_0}^{2\pi+\phi_0} \mathrm{e}^{\frac{\kappa+1}{R}\sin\theta\sqrt{\left(w_1^\star\right)^2+\left(w_2^\star\right)^2}\sin\phi}\mathrm{d}\phi$ and $\phi_0 = \arctan\dfrac{w_1^\star}{w_2^\star} + \pi(w_2^\star \le 0)$.

Because sin is a 2π-periodic function and thanks to the relation $\int_0^{2\pi} e^{z\sin x}\mathrm{d}x = 2\pi I_0(z)$, for any $z \in \mathbb{R}$, which can be deduced from [47, p. 376], we can simplify $h(\boldsymbol{w}^\star, \theta)$ to:

$$h(\boldsymbol{w}^\star, \theta) = 2\pi I_0\left(\frac{\kappa+1}{R}\sin\theta\sqrt{(w_1^\star)^2 + (w_2^\star)^2}\right) . \tag{19}$$

Substituting Eq.(19) into Eq.(18) and observing that $w_3^\star = \boldsymbol{e}_3'\boldsymbol{w}^\star = \boldsymbol{e}_3'P\boldsymbol{w} = \boldsymbol{\mu}'\boldsymbol{w}$ and $(w_1^\star)^2 + (w_2^\star)^2 = \|\boldsymbol{w}^\star\|^2 - (w_3^\star)^2 = \|\boldsymbol{w}\|^2 - (\boldsymbol{\mu}'\boldsymbol{w})^2$ yields the following single-integral representation of Q:

$$\begin{aligned} Q(\boldsymbol{w};\boldsymbol{\mu},\kappa,R) = 2\pi \int_{-1}^{1} \mathrm{e}^{\frac{\kappa}{2}t^2 + (\kappa + w_{/\!/})t} \\ \times I_0\left((\kappa+1)w_\perp\sqrt{1-t^2}\right) dt . \end{aligned} \tag{20}$$

Inserting Eq.(20) into Eq.(17) ends the proof for $f_{\mathbf{x}}$.

Let $\mathbf{y}$ be a 3-dimensional random variable whose pdf is a mixture of two equally weighted pdfs with associated probability distributions $H_{\boldsymbol{\mu},\kappa,R}$ and $H_{-\boldsymbol{\mu},\kappa,R}$ respectively. Its cf is given by:

$$\begin{aligned} \varphi_{\mathbf{y}}(\boldsymbol{t};\pm\boldsymbol{\mu},\kappa,R) &= \mathrm{e}^{-\frac{R^2}{2(\kappa+1)}\left(\|\boldsymbol{t}\|^2 + \kappa(\boldsymbol{\mu}'\boldsymbol{t})^2\right)} \\ &\times \frac{\kappa}{\operatorname{sh}\kappa}\begin{cases} \dfrac{\sin\sqrt{R^2\|\boldsymbol{t}\|^2 - \kappa^2}}{\sqrt{R^2\|\boldsymbol{t}\|^2 - \kappa^2}} & , \ \boldsymbol{t} \in \Omega , \\ \dfrac{\alpha\operatorname{sh}\alpha\cos\beta + \beta\operatorname{ch}\alpha\sin\beta}{\alpha^2+\beta^2} & , \ \boldsymbol{t} \notin \Omega , \end{cases} \end{aligned} \tag{21}$$

where α, β and Ω are given by Eq.(14).

Proof: By definition of $\mathbf{y}$, $\varphi_{\mathbf{y}}(\boldsymbol{t};\pm\boldsymbol{\mu},\kappa,R) = \frac{1}{2}\varphi_{\mathbf{w}}(\boldsymbol{t};\boldsymbol{\mu},\kappa,R) + \frac{1}{2}\varphi_{\mathbf{w}}(\boldsymbol{t};-\boldsymbol{\mu},\kappa,R)$. Moreover, it follows from Eq.(14) that $\alpha(\boldsymbol{t};-\boldsymbol{\mu},\kappa,R) = \alpha(\boldsymbol{t};\boldsymbol{\mu},\kappa,R) = \alpha$ and $\beta(\boldsymbol{t};-\boldsymbol{\mu},\kappa,R) = -\beta(\boldsymbol{t};\boldsymbol{\mu},\kappa,R) = -\beta$. We can therefore deduce that:

$$\begin{aligned} \varphi_{\mathbf{y}}(\boldsymbol{t};\pm\boldsymbol{\mu},\kappa,R) &= \mathrm{e}^{-\frac{R^2}{2(\kappa+1)}\left(\|\boldsymbol{t}\|^2 + \kappa(\boldsymbol{\mu}'\boldsymbol{t})^2\right)} \\ &\times \frac{\kappa}{\operatorname{sh}\kappa}\begin{cases} \dfrac{\sin\sqrt{R^2\|\boldsymbol{t}\|^2 - \kappa^2}}{\sqrt{R^2\|\boldsymbol{t}\|^2 - \kappa^2}} & , \ \boldsymbol{t} \in \Omega , \\ \dfrac{1}{2}\left(\dfrac{\operatorname{sh}(\alpha+i\beta)}{\alpha+i\beta} + \dfrac{\operatorname{sh}(\alpha-i\beta)}{\alpha-i\beta}\right) & , \ \boldsymbol{t} \notin \Omega , \end{cases} \end{aligned}$$

Finally, simple derivations yield:

$$\begin{aligned} \frac{\operatorname{sh}(\alpha+i\beta)}{\alpha+i\beta} + \frac{\operatorname{sh}(\alpha-i\beta)}{\alpha-i\beta} &= 2\mathrm{Re}\left(\frac{\operatorname{sh}(\alpha+i\beta)}{\alpha+i\beta}\right) \\ &= \frac{\alpha\operatorname{sh}\alpha\cos\beta + \beta\operatorname{ch}\alpha\sin\beta}{\alpha^2+\beta^2} . \end{aligned}$$

References

[1] D. Le Bihan, "Looking into the functional architecture of the brain with diffusion MRI." *Nature reviews. Neuroscience*, vol. 4, no. 6, pp. 469–80, 2003.

[2] P. T. Callaghan, C. D. Eccles, and Y. Xia, "Nmr microscopy of dynamic displacements: k-space and q-space imaging," *Journal of Physics E: Scientific Instruments*, vol. 21, no. 8, p. 820, 1988.

[3] E. O. Stejskal, "Use of Spin Echoes in a Pulsed Magnetic-Field Gradient to Study Anisotropic, Restricted Diffusion and Flow," *The Journal of Chemical Physics*, vol. 43, no. 10, pp. 3597–3603, 1965.

[4] P. T. Callaghan, *Principles of Nuclear Magnetic Resonance Microscopy*. Oxford University Press, 1991.

[5] D. C. Alexander, *An introduction to computational diffusion MRI: the diffusion tensor and beyond*, ser. Visualization and Processing of Tensor Fields. Springer Berlin Heidelberg, 2006, ch. 5, pp. 83–106.

[6] H. Gudbjartsson and S. Patz, "The Rician distribution of noisy MRI data," *Magnetic Resonance in Medicine*, vol. 34, no. 6, pp. 910–914, 1995.

[7] H.-E. Assemlal, D. Tschumperlé, L. Brun, and K. Siddiqi, "Recent advances in diffusion MRI modeling: Angular and radial reconstruction." *Medical image analysis*, 2011.

[8] D. Tuch, "Diffusion MRI of complex tissue structure," Ph.D. dissertation, 2002.

[9] V. Wedeen, T. Reese, D. Tuch, M. Weigel, J. Dou, R. Weiskoff, and D. Chessler, "Mapping fiber orientation spectra in cerebral white matter with Fourier-transform diffusion MRI," in *Proc. Intl. Sot. Mag. Reson. Med*, vol. 8, 2000, p. 82.

[10] V. J. Wedeen, R. P. Wang, J. D. Schmahmann, T. Benner, W. Y. I. Tseng, G. Dai, D. N. Pandya, P. Hagmann, H. D'Arceuil, and a. J. de Crespigny, "Diffusion spectrum magnetic resonance imaging (DSI) tractography of crossing fibers." *NeuroImage*, vol. 41, no. 4, pp. 1267–77, 2008.

[11] Y. Wu and A. Alexander, "Hybrid diffusion imaging," *NeuroImage*, vol. 36, no. 3, pp. 617–629, 2007.

[12] A. Barmpoutis, B. Vemuri, and J. Forder, "Fast displacement probability profile approximation from HARDI using 4th-order tensors," in *Biomedical Imaging: From Nano to Macro, 2008. ISBI 2008. 5th IEEE International Symposium on.* IEEE, 2008, pp. 911–914.

[13] A. Ghosh and R. Deriche, "Fast and closed-form ensemble-average-propagator approximation from the 4th-order diffusion tensor," in *Biomedical Imaging: From Nano to Macro, 2010 IEEE International Symposium on.* IEEE, 2010, pp. 1105–1108.

[14] H.-E. Assemlal, D. Tschumperlé, and L. Brun, "Efficient and robust computation of PDF features from diffusion MR signal." *Medical image analysis*, vol. 13, no. 5, pp. 715–29, 2009.

[15] J. Cheng, A. Ghosh, T. Jiang, and R. Deriche, "Model-free and analytical EAP reconstruction via spherical polar Fourier diffusion MRI." *Medical image computing and computer-assisted intervention : MICCAI ... International Conference on Medical Image Computing and Computer-Assisted Intervention*, vol. 13, no. Pt 1, pp. 590–7, 2010.

[16] M. Descoteaux, R. Deriche, D. Le Bihan, J.-F. Mangin, and C. Poupon, "Multiple q-shell diffusion propagator imaging." *Medical image analysis*, pp. 1–19, 2010.

[17] C. Liu, R. Bammer, B. Acar, and M. E. Moseley, "Characterizing non-Gaussian diffusion by using generalized diffusion tensors." *Magnetic resonance in medicine : official journal of the Society of Magnetic Resonance in Medicine / Society of Magnetic Resonance in Medicine*, vol. 51, no. 5, pp. 924–37, 2004.

[18] D. S. Tuch, T. G. Reese, M. R. Wiegell, N. Makris, J. W. Belliveau, and V. J. Wedeen, "High Angular Resolution Diffusion Imaging reveals intravoxel white matter fiber heterogeneity," *Magnetic Resonance in Medicine*, vol. 48, pp. 577–582, 2002.

[19] J. G. Malcolm, O. Michailovich, S. Bouix, C.-F. Westin, M. E. Shenton, and Y. Rathi, "A filtered approach to neural tractography using the Watson directional function," *Medical Image Analysis*, vol. 14, no. 1, pp. 58 – 69, 2010.

[20] T. E. J. Behrens, M. W. Woolrich, M. Jenkinson, H. Johansen-Berg, R. G. Nunes, S. Clare, P. M. Matthews, J. M. Brady, and S. M. Smith, "Characterization and propagation of uncertainty in diffusion-weighted MR imaging." *Magn. Res. Med.*, vol. 50, no. 5, pp. 1077–88, Nov. 2003.

[21] B. Scherrer and S. K. Warfield, "Why multiple b-values are required for multi-tensor models. Evaluation with a constrained log-euclidean model," in *IEEE ISBI'10*, 2010, pp. 1389–1392.

[22] D. Tuch, R. Weisskoff, J. Belliveau, and V. Wedeen, "High angular resolution diffusion imaging of the human brain," in *Proceedings of the 7th Annual Meeting of ISMRM*, 1999, p. 321.

[23] D. S. Tuch, "Q-ball imaging." *Magnetic resonance in medicine : official journal of the Society of Magnetic Resonance in Medicine / Society of Magnetic Resonance in Medicine*, vol. 52, no. 6, pp. 1358–72, 2004.

[24] E. Ozarslan, T. M. Shepherd, B. C. Vemuri, S. J. Blackband, and T. H. Mareci, "Resolution of complex tissue microarchitecture using the diffusion orientation transform (DOT)." *NeuroImage*, vol. 31, no. 3, pp. 1086–103, 2006.

[25] I. Aganj, C. Lenglet, G. Sapiro, E. Yacoub, K. Ugurbil, and N. Harel, "Reconstruction of the orientation distribution function in single- and multiple-shell q-ball imaging within constant solid angle." *Magnetic resonance in medicine : official journal of the Society of Magnetic Resonance in Medicine / Society of Magnetic Resonance in Medicine*, vol. 64, no. 2, pp. 554–66, 2010.

[26] A. W. Anderson, "Measurement of fiber orientation distributions using high angular resolution diffusion imaging." *Magnetic resonance in medicine : official journal of the Society of Magnetic Resonance in Medicine / Society of Magnetic Resonance in Medicine*, vol. 54, no. 5, pp. 1194–206, 2005.

[27] C. P. Hess, P. Mukherjee, E. T. Han, D. Xu, and D. B. Vigneron, "Q-ball reconstruction of multimodal fiber orientations using the spherical harmonic basis." *Magnetic resonance in medicine : official journal of the Society of Magnetic Resonance in Medicine / Society of Magnetic Resonance in Medicine*, vol. 56, no. 1, pp. 104–17, 2006.

[28] M. Descoteaux, E. Angelino, S. Fitzgibbons, and R. Deriche, "Regularized, Fast, and Robust Analytical Q-Ball Imaging," *Magn Res Med*, vol. 58, pp. 497–510, 2007.

[29] Y. Assaf, R. Z. Freidlin, G. K. Rohde, and P. J. Basser, "New modeling and experimental framework to characterize hindered and restricted water diffusion in brain white matter." *Magnetic resonance in medicine : official journal of the Society of Magnetic Resonance in Medicine / Society of Magnetic Resonance in Medicine*, vol. 52, no. 5, pp. 965–78, 2004.

[30] C. Neuman, "Spin echo of spins diffusing in a bounded medium," *Journal of Chemical Physics*, vol. 60, no. 11, pp. 4508–11, 1974.

[31] D. Healy, "Spherical Deconvolution," *Journal of Multivariate Analysis*, vol. 67, no. 1, pp. 1–22, 1998.

[32] B. Jian and B. Vemuri, "A unified computational framework for deconvolution to reconstruct multiple fibers from diffusion weighted MRI," *Medical Imaging, IEEE Transactions on*, vol. 26, no. 11, pp. 1464–1471, 2007.

[33] A. Anderson and Z. Ding, "Sub-voxel measurement of fiber orientation using high angular resolution diffusion tensor imaging," in *Book of abstracts: Tenth Annual Meeting of the International Society for Magnetic Resonance in Medicine. Berkeley, CA: ISMRM*, vol. 10, 2002, p. 440.

[34] M. Descoteaux, R. Deriche, T. R. Knösche, and A. Anwander, "Deterministic and probabilistic tractography based on complex fibre orientation distributions." *IEEE transactions on medical imaging*, vol. 28, no. 2, pp. 269–86, 2009.

[35] B. Jian, B. Vemuri, E. Ozarslan, P. Carney, and T. Mareci, "A novel tensor distribution model for the diffusion-weighted MR signal," *NeuroImage*, vol. 37, no. 1, pp. 164–176, 2007.

[36] D. Alexander, "Maximum entropy spherical deconvolution for diffusion MRI," in *Information Processing in Medical Imaging*. Springer, 2005, pp. 76–87.

[37] K. Jansons and D. Alexander, "Persistent angular structure: new insights from diffusion magnetic resonance imaging data," *Inverse problems*, vol. 19, p. 1031, 2003.

[38] J.-D. Tournier, F. Calamante, D. G. Gadian, and A. Connelly, "Direct estimation of the fiber orientation density function from diffusion-weighted MRI data using spherical deconvolution." *NeuroImage*, vol. 23, no. 3, pp. 1176–85, 2004.

[39] E. Kaden, T. R. Knï¿½sche, and A. Anwander, "Parametric spherical deconvolution: Inferring anatomical connectivity using diffusion MR imaging," *NeuroImage*, vol. 37, no. 2, pp. 474 – 488, 2007.

[40] A. Barmpoutis, B. Jian, and B. C. Vemuri, "Adaptive kernels for multi-fiber reconstruction." in *Proceedings of IPMI 2009*, vol. 21, Jan. 2009, pp. 338–49.

[41] P. J. Basser, J. Mattiello, and D. LeBihan, "MR diffusion tensor spectroscopy and imaging." *Biophysical journal*, vol. 66, no. 1, pp. 259–67, 1994.

[42] S. Merlet and R. Deriche, "Compressed Sensing for Accelerated EAP Recovery in Diffusion MRI," in *MICCAI*, 2010, p. Page 14.

[43] S. Merlet, J. Cheng, A. Ghosh, and R. Deriche, "Spherical Polar Fourier EAP and ODF Reconstruction via Compressed Sensing in Diffusion MRI," in *ISBI*, 2011.

[44] P. Jupp and K. Mardia, "A unified view of the theory of directional statistics, 1975-1988," *International Statistical Review*, vol. 57, no. 3, pp. 261–294, 1989.

[45] O. Friman and C.-F. Westin, "Uncertainty in white matter fiber tractography." *International Conference on Medical Image Computing and Computer-Assisted Intervention*, vol. 8, no. 1, pp. 107–14, 2005.

[46] W. Hager, "Updating the inverse of a matrix," *SIAM review*, vol. 31, no. 2, pp. 221–239, 1989.

[47] M. Abramowitz and I. A. Stegun, *Handbook of mathematical functions with formulas, graphs and mathematical tables*, 9th ed. Dover Publications, 1972.

[48] P. J. Basser and C. Pierpaoli, "Microstructural and physiological features of tissues elucidated by quantitative diffusion tensor MRI," *J Magn Res*, vol. 111, no. 86, pp. 209–219, 1996.

[49] S. Peled, O. Friman, F. Jolesz, and C.-F. Westin, "Geometrically constrained two-tensor model for crossing tracts in DWI," *Magn. Res. Imag.*, vol. 24, no. 9, pp. 1263–1270, 2006.

[50] E. O. Stejskal and J. E. Tanner, "Spin Diffusion Measurements: Spin Echoes in the Presence of a Time-Dependent Field Gradient," *The Journal of Chemical Physics*, vol. 42, no. 1, p. 288, 1965.

[51] R. V. Mulkern, H. Gudbjartsson, C.-F. Westin, H. P. Zengingonul, W. Gartner, C. R. G. Guttmann, R. L. Robertson, W. Kyriakos, R. Schwartz, D. Holtzman, F. A. Jolesz, and S. E. Maier, "Multi-component apparent diffusion coefficients in human brainï¿½," *NMR in Biomedicine*, vol. 12, no. 1, pp. 51–62, 1999.

[52] N. Wiest-Daesslé, S. Prima, P. Coupé, S. P. Morrissey, and C. Barillot, "Rician noise removal by non-local means filtering for low signal-to-noise ratio MRI: applications to DT-MRI," in *MICCAI*, New York, United States, 2008, pp. 171–9. [Online]. Available: http://hal.inria.fr/inserm-00332388/en

[53] M. Descoteaux, N. Wiest-Daesslé, S. Prima, C. Barillot, and R. Deriche, "Impact of Rician Adapted Non-Local Means Filtering on HARDI," in *MICCAI*, 2008, pp. 122–30. [Online]. Available: http://hal.inria.fr/inria-00423318/en

[54] M. Powell, "The NEWUOA software for unconstrained optimization without derivatives," in *Large-Scale Nonlinear Optimization*, ser. Nonconvex Optimization and Its Applications, P. Pardalos, G. Pillo, and M. Roma, Eds. Springer US, 2006, vol. 83, pp. 255–297.

[55] K. Burnham and D. Anderson, *Model Selection and Multimodel Inference: A Practical Information-Theoretic Approach*. Springer-Verlag, 2002.

[56] A. H., "A new look at the statistical model identification," *IEEE Transactions on Automatic Control*, vol. 19, pp. 716–723, 1974.

[57] J. D.K., "Determining and visualizing uncertainty in estimates of fiber orientation from diffusion tensor mri," *Magnetic Resonance in Medicine*, vol. 49, pp. 7–12, 2003.

[58] O. Söderman and B. Jönsson, "Restricted diffusion in cylindrical geometry," *J. Magn. Reson. A*, vol. 117, no. 1, pp. 94–97, 1995.

[59] S. Dégerine, "Lois de von Mises et lois liées," *Annales de l'Institut Henri Poincaré*, vol. 15, no. 1, pp. 63–77, 1979.

[60] T. Anderson, *An introduction to multivariate statistical analysis*, ser. Wiley series in probability and mathematical statistics. Probability and mathematical statistics. Wiley-Interscience, 2003.

Centre de recherche INRIA Rennes – Bretagne Atlantique
IRISA, Campus universitaire de Beaulieu - 35042 Rennes Cedex (France)

Centre de recherche INRIA Bordeaux – Sud Ouest : Domaine Universitaire - 351, cours de la Libération - 33405 Talence Cedex
Centre de recherche INRIA Grenoble – Rhône-Alpes : 655, avenue de l'Europe - 38334 Montbonnot Saint-Ismier
Centre de recherche INRIA Lille – Nord Europe : Parc Scientifique de la Haute Borne - 40, avenue Halley - 59650 Villeneuve d'Ascq
Centre de recherche INRIA Nancy – Grand Est : LORIA, Technopôle de Nancy-Brabois - Campus scientifique
615, rue du Jardin Botanique - BP 101 - 54602 Villers-lès-Nancy Cedex
Centre de recherche INRIA Paris – Rocquencourt : Domaine de Voluceau - Rocquencourt - BP 105 - 78153 Le Chesnay Cedex
Centre de recherche INRIA Saclay – Île-de-France : Parc Orsay Université - ZAC des Vignes : 4, rue Jacques Monod - 91893 Orsay Cedex
Centre de recherche INRIA Sophia Antipolis – Méditerranée : 2004, route des Lucioles - BP 93 - 06902 Sophia Antipolis Cedex

Éditeur
INRIA - Domaine de Voluceau - Rocquencourt, BP 105 - 78153 Le Chesnay Cedex (France)
http://www.inria.fr
ISSN 0249-6399